Influence of Defects on the Charge Density Wave of $([SnSe]_{1+\delta})_1(VSe_2)_1$ Ferecrystals

Matthias Falmbigl,[†] Daniel Putzky,[†] Jeffrey Ditto,[†] Marco Esters,[†] Sage R. Bauers,[†] Filip Ronning,[‡] and David C. Johnson*[,†]

[†]Materials Science Institute and Chemistry Department, University of Oregon, Eugene, Oregon 97403, United States and [‡]Los Alamos National Laboratory, Los Alamos, New Mexico 87544, United States

ABSTRACT A series of ferecrystalline compounds $([SnSe]_{1+\delta})_1(VSe_2)_1$ with varying Sn/V ratios were synthesized using the modulated elemental reactant technique. Temperature-dependent specific heat data reveal a phase transition at 102 K, where the heat capacity changes abruptly. An abrupt increase in electrical resistivity occurs at the same temperature, correlated with an abrupt increase in the Hall coefficient. Combined with the magnitude and nature of the specific heat discontinuity, this suggests that the transition is similar to the charge density wave transitions in transition metal dichalcogenides. An ordered intergrowth was formed over a surprisingly wide compositional range of Sn/V ratios of $0.89 \leq 1 + \delta \leq 1.37$. X-ray diffraction and transmission electron microscopy reveal the formation of various volume defects in the compounds in response to the nonstoichiometry. The electrical resistivity and Hall coefficient data of samples with different Sn/V ratios show systematic variation in the carrier concentration with the Sn/V ratio. There is no significant change in the onset temperature of the charge density wave transition, only a variation in the carrier densities before and after the transition. Given the sensitivity of the charge density wave transitions of transition metal dichalcogenides to variations in composition, it is very surprising that the charge density wave transition observed at 102 K for $([SnSe]_{1.15})_1(VSe_2)_1$ is barely influenced by the nonstoichiometry and structural defects. This might be a consequence of the two-dimensional nature of the structurally independent VSe_2 layers.

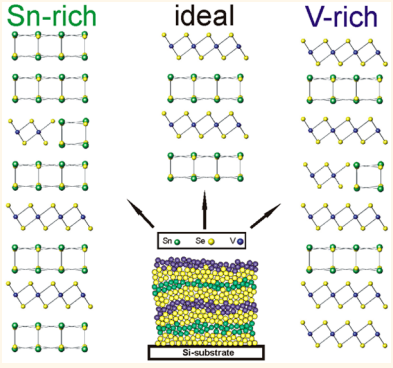

KEYWORDS: intergrowth compounds · ferecrystals · stacking defects · heat capacity · carrier concentration · charge density wave

The discovery of graphene with its unique properties[1−3] has inspired the exploration of many other candidates qualifying as two-dimensional materials, such as boron nitride,[4] transition metal dichalcogenides (TMDs),[5] and halides.[6] In the past decade, researchers have found exotic and intriguing properties in these and other two-dimensional materials, offering a wide range of electrical properties from metals to semiconductors and insulators.[2,3,6−8] The TMDs MoS_2 and WS_2 have attracted much attention due to a change from an indirect to a direct band gap upon reduction of symmetry from 3D to a 2D monolayer[5] and their potential use in optoelectronic and light-harvesting applications.[9,10] Reducing the dimensionality of metallic TMDs with charge density waves (CDWs) has theoretically been predicted to convert 2*H*-$NbSe_2$ from a metal to a semimetal,[11] to cause no change or only slight changes in the wave vector for 2*H*-$TaSe_2$,[12] and to induce the presence of magnetism in 1*T*-VSe_2 monolayers.[13] It was demonstrated that these materials have potential applications as thin film switches and in logic circuits.[14]

In 3D bulk materials, the charge density wave transition is strongly influenced and easily suppressed by any defects and impurities.[15] Partial substitution of the transition metal cation can result in a decrease[16] or an increase of the transition temperature[17] but always leads to a suppression of the charge density wave at higher substitution levels. Recently, it has been demonstrated that the charge density wave transition temperature (T_{CDW}) in transition metal dichalcogenides can be modified by varying the thickness of nanosheets without significantly affecting the magnitude of the

* Address correspondence to davej@uoregon.edu.

Received for review June 3, 2015 and accepted July 14, 2015.

Published online July 14, 2015
10.1021/acsnano.5b03361

TABLE 1. Deposition Parameter Ratio and Resulting Composition Determined by EPMA, Precursor Repeat Thickness, *a*-Axis and *c*-Axis Lattice Parameters of the Constituents and the Respective $([SnSe]_{1+\delta})_1(VSe_2)_1$ Superlattice, and the Calculated Misfit Parameter, δ

Sn/V ratio, EPMA	Sn/V ratio, shutter opening time	precursor thickness, nm	*c*-axis lattice parameter, nm	*a*-axis lattice parameter (SnSe), nm	*a*-axis lattice parameter (VSe_2), nm	misfit, δ
1.37	2.6	1.30(5)	1.1954(1)	0.5995(3) 0.5940(1)[a]	0.3413(1)	0.12 0.14[a]
1.32	2.6	1.26(5)	1.1941(3)			
1.23	2.4	1.24(5)	1.1990(1)			
1.17	2.4	1.29(5)	1.1989(2)	0.59273(4)	0.3408(1)	0.15
1.11	2.3	1.24(5)	1.1973(1)			
1.07	2.0	1.29(5)	1.20356(3)			
0.95	1.8	1.29(5)	1.20449(5)			
0.89	1.7	1.23(5)	1.20446(6)	0.5924(1)	0.3402(4)	0.14

[a] For the sample with a Sn/V ratio of 1.37, the in-plane X-ray diffraction pattern revealed two different *a*-axis lattice parameters for the SnSe constituent (see Figure 6).

CDW. Whereas an increase of T_{CDW} upon reducing dimensionality was reported for $TiSe_2$,[18] in VSe_2, the transition temperature decreases with smaller thickness, similar to the recently reported temperature dependence of the commensurate charge density wave transition of 1*T*-$TaSe_2$.[19,20] This would imply a destabilization of the CDW state in VSe_2 *via* reduction of the dimensionality. However, we reported a charge density wave transition for the compound $([SnSe]_{1.15})_1(VSe_2)_1$ with extensive rotational disorder between the SnSe bilayer and VSe_2 trilayer, which results in their average structures being independent of one another.[21] Compared to bulk VSe_2 and ultrathin films, the discontinuity in the electrical transport (electrical resistivity and Hall coefficient) is significantly enhanced. Increasing the VSe_2 thickness in $([SnSe]_{1.15})_1(VSe_2)_n$[22] to only two adjacent VSe_2 layers results in bulk-like behavior, suggesting that the phenomenon depends on having only a single, structurally independent VSe_2 layer. Due to the extensive rotational disorder, attempts to find a structural change using electron or X-ray diffraction (XRD) have been unsuccessful. To our knowledge, there is no information on the influence of defects on the charge density wave of structurally independent monolayers of any dichalcogenide.

Here we present specific heat data that clearly show a discontinuity at 102 K, centered within the temperature interval where the electrical resistivity and Hall coefficient both abruptly increase. No hysteresis is observed, and the magnitude and temperature dependence of these measurements are similar to those in previous reports of charge density wave transitions in transition metal dichalcogenides.[23,24] The magnitudes of the change in resistivity and carrier concentration in stoichiometric $([SnSe]_{1.15})_1(VSe_2)_1$ are both larger than that observed in bulk transition metal dichalcogenides. We find that the charge density wave transition temperature is not modified in $([SnSe]_{1+\delta})_1(VSe_2)_1$ as the Sn/V ratio is varied in the range $0.89 \leq 1+\delta \leq 1.37$, even though the average carrier concentration systematically changes. The magnitude of change in both resistivity and Hall coefficient is, however, strongly influenced by the Sn/V ratio. X-ray diffraction and electron microscopy investigations show that the nonstoichiometry results in partial or complete replacement of one constituent layer by the other, with the density of these stacking defects scaling with the extent of nonstoichiometry. Hence the decline in the magnitude of the change in resistivity is correlated to a change in the volume fraction of independent VSe_2 monolayers and demonstrates that the charge density wave transition in these intergrowth compounds arises from the VSe_2 constituent.

RESULTS AND DISCUSSION

Synthesis and Structural Properties. Details of the calibration process and the determination of the best conditions for the subsequent annealing step are described elsewhere.[21,25] In contrast to the previous synthesis of stoichiometric compounds of $([SnSe]_{1.15})_m(VSe_2)_n$,[21,22,25] for this study, the parameters for the amounts of Sn and V deposited onto the Si wafers were varied systematically in order to obtain precursors with different Sn/V ratios. To promote the self-assembly of the targeted compounds by annealing at 400 °C for 20 min, the precursor thickness was kept nearly constant for all compounds (see Table 1), but the relative thickness of the constituent layers was varied. The linear dependence of the ratio of the deposition times and the resulting composition is shown in Figure 1.

The XRD patterns of all samples show Bragg reflections that can be indexed as consecutive 00*l* peaks, and the superstructure is formed over a surprisingly wide range of Sn/V ratios without dramatic changes in the specular X-ray diffraction patterns (Figure 2). A closer inspection of the diffractograms displayed in Figure 2, however, reveals several distinct features as the Sn/V ratio changes from 0.89 to 1.37: (i) at high V content, all peaks appear to be symmetrically shaped, whereas for Sn-rich compounds, the peak width and asymmetry of the Bragg reflections increase; (ii) the (006) reflection is only observed below a Sn/V ratio of 1.1; (iii) as the Sn

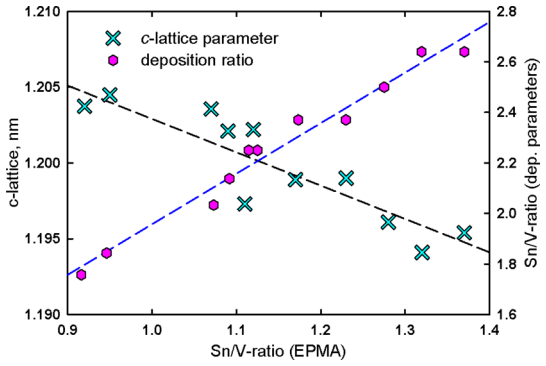

Figure 1. *c*-axis lattice parameters and ratio of the Sn/V deposition rates as a function of the measured Sn/V ratio for all $([SnSe]_{1+\delta})_1(VSe_2)_1$ compounds. The blue dashed line is a least-squares fit of (Sn deposition time)/(V deposition time) *versus* the measured Sn/V composition ratio. The black dashed line is a fit of the *c*-lattice parameters as a function of the measured Sn/V composition ratio.

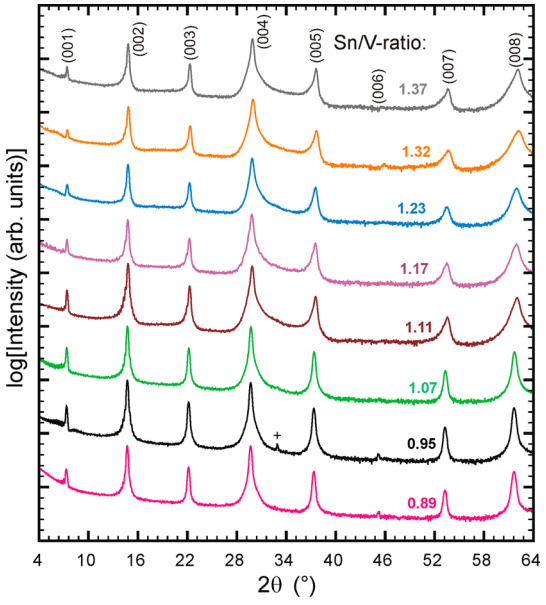

Figure 2. Specular X-ray diffraction of selected samples covering the investigated range of different Sn/V ratios. Only (00*l*) reflections are observed; + denotes the Si substrate peaks.

content increases, a broad feature around 30−35° in 2θ raises the background, which might arise from the (400) reflection of bulk SnSe[26] or the presence of amorphous material. These systematic changes confirm that the superlattice is modified as a function of the Sn/V ratio.

The lattice parameters of the compounds determined from the patterns in Figure 2 also vary linearly with the Sn/V ratio (see Figure 1). The difference in the repeat thickness of the superlattice can be explained by the different layer thicknesses along the *c*-direction for the two different constituents, 0.576(1) nm for SnSe[25] and 0.596(1) nm for VSe_2.[22] For high Sn/V ratios, a substitution of the dichalcogenide by the SnSe constituent is observed (see Figure 3), resulting in an average *c*-lattice parameter slightly smaller than that in the stoichiometric compounds. The relatively large random scatter of the *c*-axis lattice parameters around the linear trend is not unexpected, as it depends not only on the total amount of each constituent but also on the distribution of the constituents throughout the compound as the interlayer distances between the constituents vary significantly from SnSe−SnSe (0.261−0.271 nm)[25] to SnSe−VSe_2 (0.292−0.301 nm)[22] and VSe_2−VSe_2 (0.288−0.289 nm).[22]

A direct proof of these observations is shown in the high-angle annular dark-field scanning transmission electron microscopy (HAADF-STEM) images. The results for an extremely Sn-rich compound with a Sn/V ratio of 1.37 are displayed in Figure 3. Although the ideal layering sequence of alternating SnSe bilayers (brighter) and VSe_2 trilayers (darker) is still visible, additional SnSe layers are frequently replacing the VSe_2 constituent (Figure 3a). The partial replacement of layers without any obvious interruption or strain was already reported for the $([SnSe]_{1.15})_m(TaSe_2)_n$ ferecrystals.[27] These volume defects occur without deformation of involved or adjacent layers (see Figure 3b). However, as can be seen in Figure 3a, the thickness of the layers varies between the ideal stacking (1.75 nm for a sequence of SnSe−VSe_2−SnSe) and the defect stacking (1.73 nm for three consecutive SnSe layers). These values are in excellent agreement with the expected values of 1.748 and 1.728 nm, respectively, using the *c*-axis lattice parameters for the two different constituents. It is interesting to note that most layers of the defect blocks (three consecutive SnSe layers) show all the same orientation, corresponding to the (100) orientation of a rocksalt structured layer. For the VSe_2 layer, several times a (110) orientation indicating an octahedral coordination of the V atom similar to the bulk 1*T* structure is observed (see Figure 3c). An inspection of larger areas of the compound clearly reveals no long-range order between the stacking defects.

In Figure 4, HAADF-STEM images of the compound with the highest V content are displayed. Also, the ideal alternating layering sequence is interrupted by the insertion and substitution of several VSe_2 layers replacing SnSe layers (see Figure 4a). The thickness of three consecutive layers of VSe_2 is 1.79(1) nm, which is in good agreement with the sum of three monolayers of 0.596(1) nm reported for $([SnSe]_{1.15})_1(VSe_2)_n$ compounds.[22] In Figure 4b, a transition from the brighter SnSe layer into the darker dichalcogenide layer is highlighted. Again, this local substitution takes place without any significant distortion around this area. In Figure 4c, distinct crystallographic orientations of both constituents can be identified.

Rietveld refinements for these compounds were based on the information gained from the analysis of the HAADF-STEM images to create a layer substitution model. Starting from the ideal (1,1) superstructures,

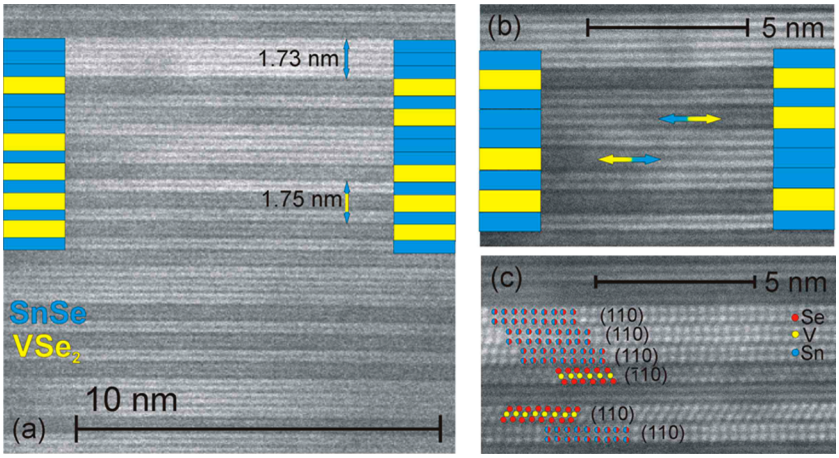

Figure 3. HAADF-STEM image of the sample with a Sn/V ratio of 1.37. The partial replacement of the dichalcogenide layer by SnSe layers is observed (a). The stacking defects (b) and respective crystallographic orientations of the constituent layers (c) are highlighted.

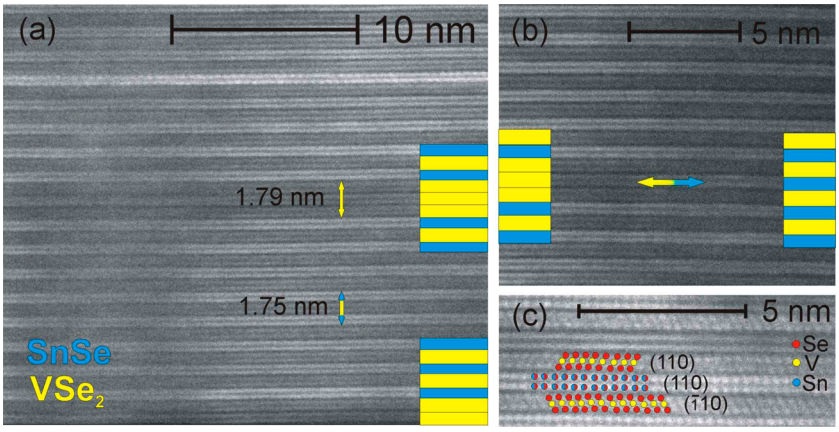

Figure 4. HAADF-STEM image of the compound with a Sn/V ratio of 0.89. The partial replacement of the SnSe layers with VSe_2 layers is observed (a). The stacking defects (b) and respective crystallographic orientations of the constituent layers (c) are highlighted.

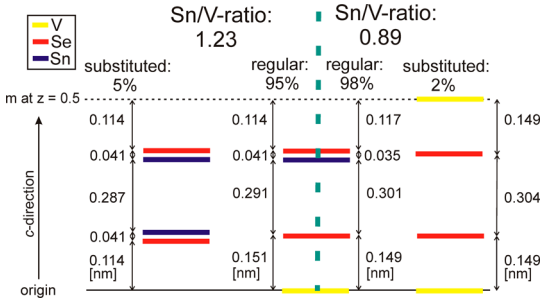

Figure 5. Rietveld refinement results for a substitution model, where one of the constituent layers is partially replaced by the other one for two compounds with Sn/V ratios of 1.23 and 0.89, respectively. The refinement reveals interplanar distances along the *c*-axis. The error in all distances is below 0.005 nm.

partial layer substitution of either the SnSe or the VSe_2 constituent was introduced to mimic the complex scenario present in these compounds (Figure 5). First, the ideal (1,1) structure was refined, followed by introducing the substitution model according to the Sn/V ratio. The distances within two similar layers were constrained to be the same, while only the occupation was refined to keep the number of refinable parameters reasonably low. For both compounds with a Sn/V ratio of 1.23 and 0.89, respectively, the introduction of the substitution model resulted in a significant lowering of the *R* values. The resulting distances in the superlattices along the *c*-axis are plotted in Figure 5 and show that the portion representing the ideal stacking sequence is very similar in both cases. One noteworthy result is that the average spacing between the layers is slightly larger in case of the V-rich sample, which can be attributed to the presence of weaker bonding between two VSe_2 layers and VSe_2 and SnSe compared to two consecutive rocksalt structured layers with strong ionic bonding. The model reveals a Sn/V ratio of 1.21 for the Sn-rich sample, which is in excellent agreement with the electron probe microanalyzer (EPMA) result of 1.23; however, for the V-rich sample, the refinement results in a ratio of 1.1, which is too high compared to 0.89 from EPMA. This might be

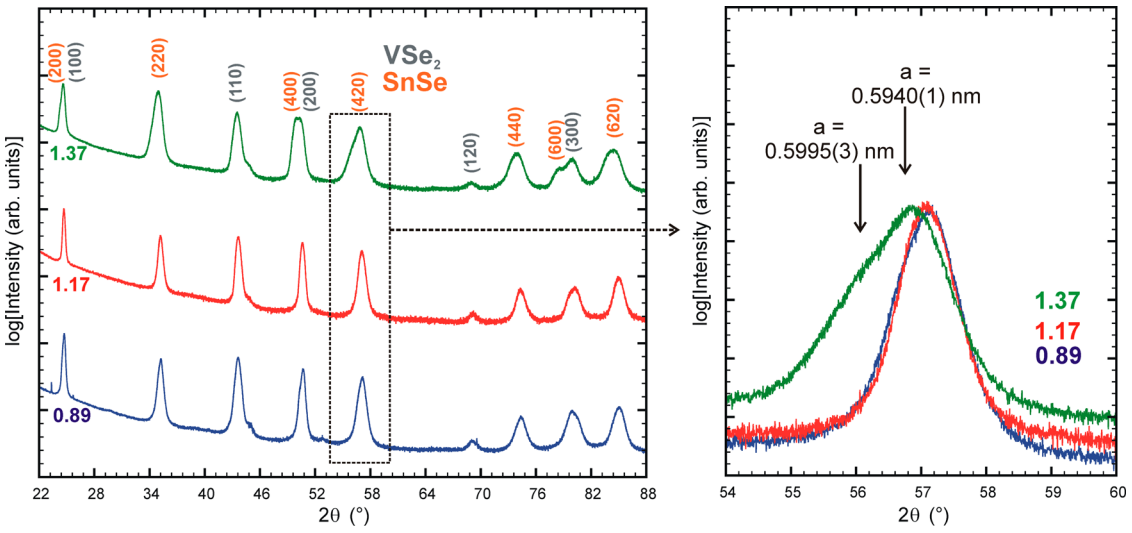

Figure 6. In-plane X-ray diffraction patterns for three compounds with Sn/V ratios of 0.89, 1.17, and 1.37. The (*hk*0) indices of the rocksalt and dichalcogenide structures are provided, and the (420) peak of the SnSe constituent is magnified to highlight the presence of two different lattice dimensions for the Sn-rich sample.

caused by the nonuniform distribution of the additional VSe_2 layers or the restrictions and limitations of the substitution model.

In-plane X-ray diffraction was conducted for three samples with Sn/V ratios of 0.89, 1.17, and 1.37. The patterns are displayed in Figure 6 and reveal peaks corresponding to the crystal structure of the individual constituents as typically observed for ferecrystalline compounds.[28] The peaks of the SnSe constituent can be indexed to the square basal plane of a rocksalt structure, and the peaks attributed to the VSe_2 constituent are consistent with a hexagonal basal plane of the 1*T* bulk structure.[29] The lattice parameters of the SnSe and VSe_2 constituents are listed in Table 1 and are consistent with the ones reported earlier for $([SnSe]_{1.15})_m(VSe_2)_n$ ferecrystalline compounds.[21,22,25] One interesting observation is that for the Sn-richest compound each Bragg peak of the SnSe constituent exhibits a splitting. This clearly points toward the presence of two distinct in-plane lattice parameters for this constituent. Interestingly, the peaks at slightly lower angles corresponding to a larger *a*-axis lattice parameter of 0.5995(3) nm exhibit lower intensity and can thus be attributed to the inserted SnSe, where three or more consecutive layers are present (see Figure 3a). Indeed, the in-plane lattice parameter of $([SnSe]_{1.15})_m(VSe_2)_1$ with $m = 2$ and 3 is slightly increased compared to the compound with only one SnSe layer ($m = 1$, $a = 0.5935(4)$ nm) and range between 0.59923(7) and 0.59976(2) nm.[25] In general, the in-plane lattice parameters of both constituents increase slightly as the Sn content is increased (see Table 1).

Specific Heat. The temperature-dependent specific heat of a compound with Sn/V ratio of 1.17 is displayed in Figure 7. Figure 7a shows the temperature dependence compared to that of bulk VSe_2.[23] In both cases, the heat capacity at 200 K approaches, but remains below, the Dulong-Petit value. Similar to the VSe_2, which shows a discontinuity at 110 K,[23] a jump in the specific heat at 102 K (see inset Figure 7a) is observed for the ferecrystalline compound $([SnSe]_{1.15})_1(VSe_2)_1$. In both cases, this anomaly can be attributed to the charge density wave transition. The specific heat below 10 K is plotted as C_P/T *versus* T^2, and a least-squares fit to the equation given in Figure 7b is plotted. The fit reveals an electronic Sommerfeld coefficient (γ) of 24.5 mJ mol^{-1} K^{-2} and a Debye temperature of θ_D = 185.5 K, which was calculated according to

$$\beta = \frac{12nR\pi^4}{5\theta_D{}^3} \qquad (1)$$

where n is the number of atoms per formula unit and R is the gas constant. This value is slightly smaller than θ_D = 213 K for bulk VSe_2[23] and $\theta_D \sim 200-300$ K for sulfur-based misfit layer compounds.[30,31] However, the electronic specific heat is significantly larger than the 7 mJ mol^{-1} K^{-2} reported for bulk VSe_2.[23] This might result from a significant contribution of the SnSe constituent. The size of the specific heat jump (ΔC_P) at the CDW transition can be used to estimate the density of electronic states ($D_\uparrow(E_F)$) removed by the formation of gaps at the Fermi surface. $\Delta C_P \sim 1.8$ J mol^{-1} K^{-1} is on the same order of magnitude as that reported for the transition in bulk $TiSe_2$, where the anomaly is $\Delta C_P \sim 1.15$ J mol^{-1} K^{-1}.[24] Assuming a distribution of local gap sizes with a temperature dependence as in the BCS theory of superconductors, McMillan derived the following expression for the size of the specific heat jump at a CDW transition:[32]

$$\Delta C_P = 3 \times 9.4 D_\uparrow(E_F) k_B{}^2 T_C \qquad (2)$$

Applying eq 2 results in $D_\uparrow(E_F)$ = 0.87 states/eV − V atom − spin (for one spin direction), which is well within the range reported for various transition metal

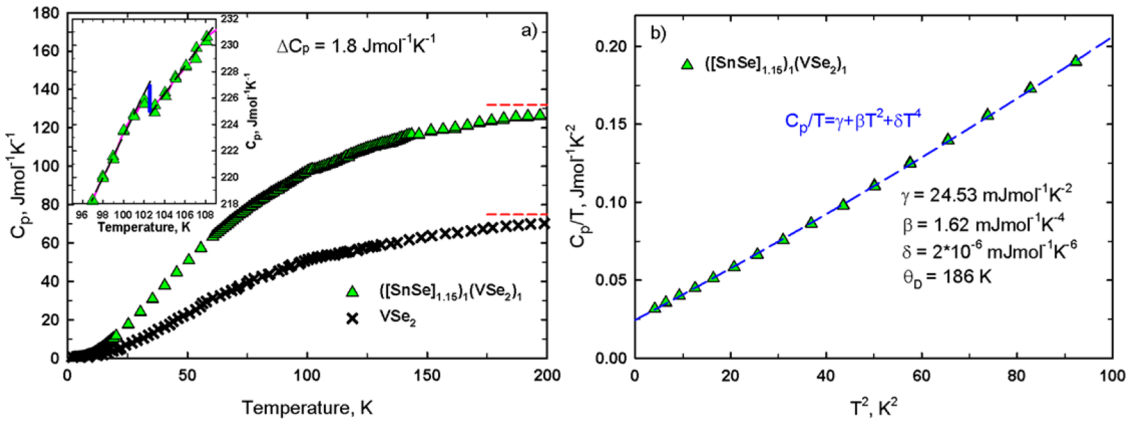

Figure 7. (a) Heat capacity (C_P) of $([SnSe]_{1.15})_1(VSe_2)_1$, compared to single-crystalline VSe_2[23] as a function of temperature. The red dashed lines indicate the classic Dulong-Petit value for vibrations. The inset shows a discontinuity at 102 K, which is attributed to the charge density wave transition. (b) C_P/T *vs* T^2 for $([SnSe]_{1.15})_1(VSe_2)_1$ below 10 K, including a least-squares fit (blue dashed line) to the polynomial equation given in the figure.

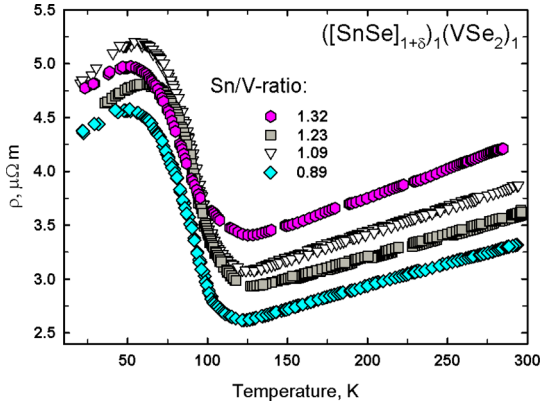

Figure 8. Electrical resistivity as a function of temperature for selected samples.

diselenides.[24] The transition is most likely of second order because, in two consecutive runs, no hysteresis during cooling or heating was observed. This is consistent with the expected transition from a normal state into the incommensurate CDW state[16] for a typical CDW unstable layered compound. In general, the anomaly found in the ferecrystalline compound $([SnSe]_{1.15})_1(VSe_2)_1$ exhibits features similar to those of the CDW transitions in single-crystalline bulk VSe_2 and $TiSe_2$.[23,24]

Transport Properties. The electrical resistivity as a function of temperature for compounds with varying Sn/V ratios is plotted in Figure 8. All compounds exhibit a charge density wave transition consistent with the results from the specific heat measurements. A minimum resistivity around 122−127 K, which increases with increasing Sn/V ratio (see Table 2), is observed. The ρ_{max}/ρ_{min} ratio increases as the compounds become richer in V and, therefore, contain a larger number of VSe_2 layers. However, the room temperature resistivity does not exhibit a systematic change, which might arise from slight variations in defect concentration and distribution and/or amount of impurities in different samples.

TABLE 2. Room Temperature Resistivity (ρ_{RT}), Temperature at ρ_{min} (T_{min}), ρ_{max}/ρ_{min}, Carriers/V Atom at Room Temperature ($n_{V,RT}$), Carriers Quenched in the CDW Transition/V Atom (n_{CDW}), and Carrier Mobility at Room Temperature (μ_{RT}) for Compounds with Different Sn/V Ratios

Sn/V ratio	ρ_{RT}, $\mu\Omega$m	T_{min}, K	ρ_{max}/ρ_{min}	$n_{V,RT}$	n_{CDW}	μ_{RT}, cm^2 V^{-1} s^{-1}
1.32	4.21	127	1.46	0.26	0.20	6.93
1.23	3.60	127	1.64	0.37	0.32	5.69
1.09	3.87	125	1.67	0.49	0.54	3.95
0.89	3.32	122	1.74	0.84	1.11	2.72

The carrier concentration, which is displayed in Figure 9, was calculated from Hall measurements by applying the single parabolic band approximation, which can only serve as a simple approach because the electronic structure of binary VSe_2 is already very complex with overlapping V d-bands and Se p-bands.[33] The Hall coefficient for all compounds was positive in the measured temperature range, suggesting that holes are the majority carriers, while electrons are found to be the majority carriers in bulk VSe_2. A systematic trend is observed in the magnitude of the Hall coefficient, with the carrier concentration decreasing as the Sn/V ratio increases. This is consistent with the structural changes where more and more metallic VSe_2 layers are replaced by semiconducting SnSe layers. A dramatic decrease of carrier concentration for all compounds at the charge density wave transition is observed; however, again, the magnitude of the change depends on the Sn/V ratio. Calculating the volume per V atom of an ideal (1,1) sample using the lattice dimensions given in Table 1 yields the number of carriers per V atom (n_V) listed in Table 2 for room temperature and the difference between the maximum and the minimum at the CDW transition. A comparison clearly shows that the change in the Sn/V ratio is too small to account for the differences observed in the carrier concentration.

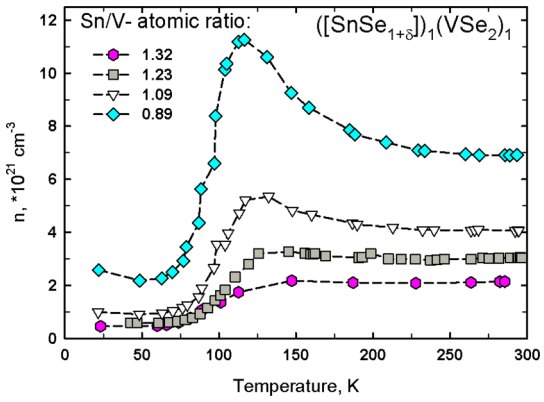

Figure 9. Carrier concentration as a function of temperature for selected samples.

Whereas the Sn/V ratio only changes by a factor of ~1.5 between the Sn- and V-richest samples, the change in the number of carriers/V exceeds 3 at room temperature and 5.5 for the carriers quenched during the CDW transition. This observation points toward more complex charge transfer mechanisms depending on the thickness of the SnSe layer (m), which were already reported for $([SnSe]_{1.15})_m(VSe_2)_1$,[25] $([PbSe]_{1.14})_m(NbSe_2)_1$,[34] and $([SnSe]_{1.16})_m(NbSe_2)_1$[35] ferecrystalline compounds and analogous misfit layer compounds.[31] Interestingly, for samples with a lower Sn/V ratio than the ideal value of 1.15, the number of carriers quenched during the transition is larger than the room temperature value, maybe indicating that at elevated temperatures minority carriers from the SnSe constituent also contribute to the Hall coefficient.

The carrier mobility values at room temperature for samples with varying Sn/V ratio are listed in Table 2. The mobility increases as a function of the Sn/V ratio, which is surprising considering that the more conducting layer is VSe_2 and that with increasing Sn/V ratio a larger number of SnSe layers are partially replacing the dichalcogenide layers. This observation might again indicate that the approximation of a single band model is not valid for these complex intergrowth compounds.

All results clearly demonstrate that the VSe_2 constituent in $([SnSe]_{1+\delta})_1(VSe_2)_1$ ferecrystals causes the charge density wave transition as the magnitude changes systematically with the number of VSe_2 layers in the compounds. However, the results from an earlier investigation on $([SnSe]_{1.15})_1(VSe_2)_n$ demonstrated that the nature of the transition changes dramatically as soon as adjacent VSe_2 layers are present and the two-dimensionality is reduced[22] and that spacing out the VSe_2 layers by more than one SnSe layer also causes changes due to charge transfer between the two constituents,[25] which overall creates a very complex scenario. The volume defects generated by varying the Sn and V content in the compounds do not suppress the charge density wave transition, rather they modify slightly the Fermi level and, hence, cause variations in the carrier concentration.

CONCLUSIONS

A series of $([SnSe]_{1+\delta})_1(VSe_2)_1$ compounds with varying Sn/V ratios was synthesized. The compounds form over a wide compositional range of Sn/V ratios from $0.89 \leq \delta \leq 1.37$. X-ray diffraction reveals systematic changes in intensity and a slight decrease of the c-axis lattice parameter as the Sn/V ratio is increased. Typical for ferecrystalline compounds, independent in-plane crystal symmetries for both constituents of the intergrowth compound were observed. The a-lattice parameter of the VSe_2 constituent increases slightly as the Sn/V ratio is increased, and the SnSe constituent exhibits two individual a-lattice parameters for individual and blocks of the rocksalt-like layer when the dichalcogenide layer is replaced or substituted. HAADF-STEM images clearly show how the mechanism of off-stoichiometry is accommodated: partial or full replacement of one layer by the other one without distortion of the surrounding layers. The temperature-dependent specific heat shows an anomaly at 102 K, which is attributed to a charge density wave transition consistent with the electrical properties. The features of the anomaly are very similar to the anomalies reported for transition metal diselenides at the CDW transition. Electrical resistivity of compounds with varying Sn/V ratio shows that only the magnitude of the CDW transition is influenced by the defects, but the CDW transition temperature is not shifted by the volume defects present in the compounds. The carrier concentration trends with the Sn/V ratio, demonstrating that the VSe_2 constituent mainly contributes to the conduction and the charge density wave of the ferecrystalline compounds. However, the change in magnitude reveals that a more complex mechanism involving charge transfer between the constituents plays a key role. The robustness of the charge density wave transition against structural defects together with the extremely low lattice thermal conductivity[36] could make these intergrowth compounds good candidates for thermal switches.

METHODS

All thin film samples were synthesized using physical vapor deposition (PVD) in a custom-built vacuum deposition chamber[37] at pressures as low as 2×10^{-7} mbar. During the deposition process, the low pressure was maintained by a cryogenic absorber pump. Se (Alfa Aesar, 99.999% purity) was evaporated utilizing an effusion cell, and electron beam guns were used to evaporate Sn (Alfa Aesar, 99.98%) and V (Alfa Aesar 99.7%). The PVD process was carried out using two different substrates, either (100)-oriented Si wafers for structural

characterizations or fused silica for the measurement of electrical properties. Details on the operation of the deposition system and the calibration procedure for the initial precursor films of the desired layered samples are described elsewhere.[21,25] All samples were annealed on a hot plate inside a glovebox under a nitrogen atmosphere (<1 ppm/O_2).

X-ray reflection (XRR) and high-resolution XRD were performed using a Bruker D8 Discover diffractometer equipped with Cu Kα radiation. High-quality scans for Rietveld refinement were collected using off-specular conditions (angle offset between θ and 2θ was in all cases 0.2°). The FullProf program package[38] was used for Rietveld refinements. In-plane diffraction of selected samples was performed at the Advanced Photon Source (APS), Argonne National Laboratories, at Beamline 33BM, using an incident X-ray beam with $\lambda = 0.12653$ nm.

The chemical composition of the thin film samples was determined using a Cameca SX100 electron probe microanalyzer equipped with five wavelength-dispersive spectrometers. A thin film technique applying three different acceleration voltages (10, 15, and 20 kV) described in detail elsewhere[39] was utilized for precise compositional analysis.

High-resolution scanning transmission electron microscopy (HRSTEM) was carried out on a FEI Titan 80-300 TEM/STEM instrument, using an objective lens c_s-correction and a HAADF detector. The preparation of selected samples for HRSTEM was performed at the Center for Advanced Materials Characterization in Oregon (CAMCOR) of the University of Oregon utilizing a FEI Helios Nanolab 600 dual-beam focused ion beam. After an *in situ* lift out, the samples were treated by a thinning technique followed by low-voltage ion beam polishing.

The sample for the heat capacity measurement was deposited onto poly(methyl methacrylate) (PMMA)-coated Si wafers, and ~5 mg of the ferecrystalline thin film material was floated off the substrate by dissolving the PMMA in acetone, followed by a drying step. Annealing of the powder was conducted in a Netzsch DSC under N_2 atmosphere. The sample was then pressed into a pellet for the heat capacity measurement done using a thermal relaxation method in a Quantum Design PPMS system. A critical examination of this technique and the accuracy for small sample masses was conducted by Lashley *et al.*[40]

In order to perform in-plane electrical resistivity and Hall measurements, a shadow mask creating a cross pattern was used during deposition. The total film thickness used for the conversion of the measured sheet resistance to electrical resistivity and the Hall coefficient was evaluated from XRR data and was for all samples about 50 nm. Small indium pieces were used to electrically contact the samples to Cu wires. All measurements were carried out in a temperature range between 20 and 295 K, and for the Hall measurements, magnetic fields up to 1.6 T were applied.

Conflict of Interest: The authors declare no competing financial interest.

Supporting Information Available: Detailed information on the Rietveld refinement results. The Supporting Information is available free of charge on the ACS Publications website at DOI: 10.1021/acsnano.5b03361.

Acknowledgment. The authors acknowledge support from the National Science Foundation under Grant DMR-1266217. M. F., J.D., M.E., and S.R.B. acknowledge support from the National Science Foundation through CCI Grant Number CHE-1102637. F.R, was supported under the auspices of the Department of Energy, Office of Basic Energy Sciences, Division of Materials Science and Engineering. Use of the Advanced Photon Source was supported by the U.S. Department of Energy, Office of Science, and the Office of Basic Energy Sciences, under Contract No. DE-AC02-06CH11357. Grant MRI 0923577 provided funding for the dual-beam focused ion beam used to make TEM cross sections.

REFERENCES AND NOTES

1. Novoselov, K. S.; Geim, A. K.; Morozov, S. V.; Jiang, D.; Zhang, Y.; Dubonos, S. V.; Grigorieva, I. V.; Firsov, A. A. Electric Field Effect in Atomically Thin Carbon Films. *Science* **2004**, *306*, 666–669.
2. Novoselov, K. S.; Geim, A. K.; Morozov, S. V.; Jiang, D.; Katsnelson, M. I.; Grigorieva, I. V.; Dubonos, S. V.; Firsov, A. A.Two-dimensional Gas of Massless Dirac Fermions in Graphene. *Nature* **2005**, *438*, 197–200.
3. Singh, V.; Joung, D.; Zhai, L.; Das, S.; Khondaker, S. I.; Seal, S. Graphene Based Materials: Past, Present and Future. *Prog. Mater. Sci.* **2011**, *56*, 1178–1271.
4. Golberg, D.; Bando, Y.; Huang, Y.; Terao, T.; Mitome, M.; Tang, C.; Zhi, C. Boron Nitride Nanotubes and Nanosheets. *ACS Nano* **2010**, *4*, 2979–2993.
5. Chhowalla, M.; Shin, H.-S.; Eda, G.; Li, L.-J.; Loh, K.-P.; Zhang, H. The Chemistry of Two-Dimensional Layered Transition Metal Dichalcogenide Nanosheets. *Nat. Chem.* **2013**, *5*, 263–275.
6. Miro, P.; Audiffred, M.; Heine, T. An Atlas of Two-Dimensional Materials. *Chem. Soc. Rev.* **2014**, *43*, 6537.
7. Balandin, A. A.; Ghosh, S.; Bao, W.; Calizo, I.; Teweldebrhan, D.; Miao, F.; Lau, C. N. Superior Thermal Conductivity of Single-Layer Graphene. *Nano Lett.* **2008**, *8*, 902–907.
8. Lee, C.; Wei, X.; Kysar, J. W.; Hone, J. Measurement of the Elastic Properties and Intrinsic Strength of Monolayer Graphene. *Science* **2008**, *321*, 385–388.
9. Eda, G.; Yamaguchi, H.; Voiry, D.; Fujita, T.; Chen, M.; Chhowalla, M. Photoluminescence from Chemically Exfoliated MoS_2. *Nano Lett.* **2011**, *11*, 5111–5116.
10. Hong, X.; Kim, J.; Shi, S. F.; Zhang, Y.; Jin, C.; Sun, Y.; Tongay, S.; Wu, J.; Zhang, Y.; Wang, F. Ultrafast Charge Transfer in Atomically Thin MoS_2/WS_2 Heterostructures. *Nat. Nanotechnol.* **2014**, *9*, 682–686.
11. Calandra, M.; Mazin, I. I.; Mauri, F. Effect of Dimensionality on the Charge-Density Wave in Few-layer 2*H*-$NbSe_2$. *Phys. Rev. B: Condens. Matter Mater. Phys.* **2009**, *80*, 241108.
12. Ge, Y.; Liu, A. Y. Effect of Dimensionality and Spin-orbit Coupling on Charge-Density-Wave Transition in 2*H*-$TaSe_2$. *Phys. Rev. B: Condens. Matter Mater. Phys.* **2012**, *86*, 104101.
13. Ma, Y.; Dai, Y.; Guo, M.; Niu, C.; Zhu, Y.; Huang, B. Evidence of the Existence of Magnetism in Pristine VX_2 Monolayers (X = S, Se) and Their Strain-Induced Tunable Magnetic Properties. *ACS Nano* **2012**, *6*, 1695–1701.
14. Renteria, J.; Samnakay, R.; Jiang, C.; Pope, T. R.; Goli, P.; Yan, Z.; Wickramaratne, D.; Salguero, T. T.; Khitun, A. G.; Lake, R. K.; et al. All-Metallic Electrically Gated 2*H*-$TaSe_2$ Thin-film Switches and Logic Circuits. *J. Appl. Phys.* **2014**, *115*, 034305.
15. Mutka, H.Advances in the Crystallographic and Microstructural Analysis of Charge Density Wave Modulated Crystals. *Physics and Chemistry of Materials with Low-Dimensional Structures*; Springer: Berlin, 1999; Vol. 22, pp 153−184.
16. Di Salvo, F. J.; Moncton, D. E.; Waszczak, J. V. Charge Density Waves in Layered Compounds. *Phys. Rev. B* **1976**, *14*, 4321.
17. Schneemeyer, L. F.; Sienko, M. J. Electric and Magnetic Anomalies at the Charge-Density-Wave Transition in Niobium-Substituted Vanadium Diselenides. *J. Phys. Chem. Solids* **1980**, *41*, 929–933.
18. Goli, P.; Khan, J.; Wickramaratne, D.; Lake, R. K.; Balandin, A. A. Charge Density Waves in Exfoliated Films of van der Waals Materials: Evolution of Raman Spectrum in $TiSe_2$. *Nano Lett.* **2012**, *12*, 5941–5945.
19. Yang, J.; Wang, W.; Liu, Y.; Du, H.; Ning, W.; Zheng, G.; Jin, C.; Han, Y.; Wang, N.; Yang, Z.; et al. Thickness Dependence of the Charge-Density-Wave Transition Temperature in VSe_2. *Appl. Phys. Lett.* **2014**, *105*, 063109.
20. Samnakay, R.; Wickramaratne, D.; Pope, T. R.; Lake, R. K.; Salguero, T. T.; Balandin, A. A. Zone-Folded Phonons and the Commensurate-Incommensurate Charge-Density-Wave Transition in 1*T*-$TaSe_2$ Thin Films. *Nano Lett.* **2015**, *15*, 2965–2973.
21. Atkins, R.; Disch, S.; Jones, Z.; Haeusler, I.; Grosse, C.; Fischer, S. F.; Neumann, W.; Zschack, P.; Johnson, D. C. Synthesis, Structure and Electrical Properties of a New Tin Vanadium Selenide. *J. Solid State Chem.* **2013**, *202*, 128–133.
22. Falmbigl, M.; Fiedler, A.; Atkins, R. E.; Fischer, S. F.; Johnson, D. C. Suppressing a Charge Density Wave by

Changing Dimensionality in the Ferecrystalline Compounds $([SnSe]_{1.15})_1(VSe_2)_n$ with n = 1, 2, 3, 4. *Nano Lett.* **2015**, *15*, 943–948.
23. Yadav, C. S.; Rastogi, A. K. Electronic Transport and Specific Heat of 1*T*-VSe_2. *Solid State Commun.* **2010**, *150*, 648–651.
24. Craven, R. A.; Di Salvo, F. J.; Hsu, F. S. L. Mechanisms for the 200K Transition in $TiSe_2$: A Measurement of the Specific Heat. *Solid State Commun.* **1978**, *25*, 39–42.
25. Atkins, R.; Dolgos, M.; Fiedler, A.; Grosse, C.; Fischer, S. F.; Rudin, S. P.; Johnson, D. C. Synthesis and Systematic Trends in Structure and Electrical Properties of $[(SnSe)_{1.15}]_m(VSe_2)_1$, m = 1, 2, 3, and 4. *Chem. Mater.* **2014**, *26*, 2862–2872.
26. Chattopadhyay, T.; Pannetier, J.; von Schnering, H. G. Neutron Diffraction Study of the Structural Phase Transition in SnS and SnSe. *J. Phys. Chem. Solids* **1986**, *170*, 29–32.
27. Grosse, C.; Atkins, R.; Krimse, H.; Mogilatenko, A.; Neumann, W.; Johnson, D. C. Local Structure and Defect Chemistry of $[(SnSe)_{1.15}]_m(TaSe_2)$ ferecrystals - A New Type of Layered Intergrowth Compound. *J. Alloys Compd.* **2013**, *579*, 507–515.
28. Beekman, M.; Heideman, C. L.; Johnson, D. C. Ferecrystals: Non-Epitaxial Layered Intergrowths. *Semicond. Sci. Technol.* **2014**, *29*, 064012.
29. Rigoult, J.; Guidi-Morosini, C.; Tomas, A.; Molinie, P. An Accurate Refinement of 1*T*-VSe_2 at Room Temperature. *Acta Crystallogr., Sect. B: Struct. Crystallogr. Cryst. Chem.* **1982**, *38*, 1557–1559.
30. Rouxel, J.; Meerschaut, A.; Wiegers, G. A. Chalcogenide Misfit Layer Compounds. *J. Alloys Compd.* **1995**, *229*, 144–157.
31. Wiegers, G. A. Charge Transfer between Layers in Misfit Layer Compounds. *J. Alloys Compd.* **1995**, *219*, 152–156.
32. McMillan, W. L. Microscopic Model of Charge-Density Waves in 2*H*-$TaSe_2$. *Phys. Rev. B* **1977**, *16*, 643.
33. Zunger, A.; Freeman, A. J. Electronic Structure of 1*T*-VSe_2. *Phys. Rev. B: Condens. Matter Mater. Phys.* **1979**, *19*, 6001–6009.
34. Alemayehu, M. B.; Mitchson, G.; Ditto, J.; Hanken, B. E.; Asta, M.; Johnson, D. C. Charge Transfer between PbSe and $NbSe_2$ in $[(PbSe)_{1.14}]_m(NbSe_2)$ Ferecrystalline Compounds. *Chem. Mater.* **2014**, *26*, 1859–1866.
35. Alemayehu, M. B.; Falmbigl, M.; Ta, K.; Grosse, C.; Westover, R. D.; Bauers, S. R.; Fischer, S. F.; Johnson, D. C. Structural and Electrical Properties of $([SnSe]_{1+\delta})_m(NbSe_2)_1$ Compounds: Single $NbSe_2$ Layers Separated by Increasing Thickness of SnSe. *Chem. Mater.* **2015**, *27*, 867–875.
36. Chiritescu, C.; Cahill, D. G.; Nguyen, N.; Johnson, D.; Bodapati, A.; Keblinski, P.; Zschack, P. Ultralow Thermal Conductivity in Disordered, Layered WSe_2 Crystals. *Science* **2007**, *315*, 351–353.
37. Fister, L.; Li, X.; McConnell, J.; Novet, T.; Johnson, D. C. Deposition System for the Synthesis of Modulated, Ultrathin-Film Composites. *J. Vac. Sci. Technol., A* **1993**, *11*, 3014–3019.
38. Roisnel, T.; Rodriguez-Carvajal, J. WinPLOTR: A Windows Eool for Powder Diffraction Pattern Analysis. *Mater. Sci. Forum* **2001**, *118*, 378–381.
39. Phung, T.; Jensen, J.; Johnson, D. C.; Donovan, J. J.; McBurnett, B. G. Determination of the Composition of Ultra-Thin Ni-Si Films on Si: Constrained Modeling of Electron Probe Microanalysis and X-Ray Reflectivity Data. *X-Ray Spectrom.* **2008**, *37*, 608–614.
40. Lashley, J. C.; Hundley, M. F.; Migliori, A.; Sarrao, J. L.; Pagliuso, P. G.; Darling, T. W.; Jaime, M.; Cooley, J. C.; Hults, W. L.; Morales, L.; et al. Critical Examination of Heat Capacity Measurements made on a Quantum Design Physical Property Measurement System. *Cryogenics* **2003**, *43*, 369–378.